Empowering Offshore Wind with ES-STATCOM for Stability Margin Improvement and Provision of Grid-Forming Capabilities

Anant Narula, Paul Imgart, Massimo Bongiorno and Mebtu Beza
Division of Electric Power Engineering
Chalmers University of Technology
Göteborg, Sweden
{anant.narula, paul.imgart, massimo.bongiorno, mebtu.beza}@chalmers.se

***Abstract*—Offshore wind power plants (WPPs) play a pivotal role in achieving a CO2-neutral electricity sector. However, their grid connection presents significant challenges and costs. High-voltage alternating current (HVAC) offers a cost-effective solution, but it may necessitate the installation of a static synchronous compensator (STATCOM) at the onshore bus to ensure stability and compliance with connection requirements. Integrating energy storage into the STATCOM (ES-STATCOM) enables the provision of ancillary services, such as inertial response and frequency support, which require active power. This paper utilizes the generalized Nyquist criterion to demonstrate that operating the ES-STATCOM with grid-forming control enhances the stability margin of the grid-connected WPP when compared to operating it with grid-following control. Furthermore, it illustrates through network frequency perturbation (NFP) plots that the overall WPP, comprising grid-following wind turbines and a grid-forming ES-STATCOM, imparts grid-forming behavior at the grid-connection point.**

***Index Terms*—Grid-forming converter, NFP plot, offshore wind power plant, small-signal stability, STATCOM.**

I. Introduction

Decarbonizing global electrical power systems, primarily through the widespread adoption of renewable energy sources such as wind, solar, tidal, and wave power, is a pivotal component in limiting global temperature increases. Wind power, in particular, has witnessed remarkable growth over the past two decades [1]. According to data from the Global Wind Energy Council, onshore wind capacity has surged from 195 GW in 2010 to 842 GW in 2022. Concurrently, offshore wind capacity has experienced even more substantial growth, escalating from 3 GW in 2010 to 64 GW in 2022, with a projected addition of 130 GW between 2023 and 2027 [2]. The expansion of offshore wind power can be attributed to its superior generation capacity and more consistent wind conditions when compared to onshore installations.

However, the remote locations of some offshore wind power plants (WPPs), located tens or even hundreds of kilometers from the nearest shore, pose significant challenges when it comes to connecting to onshore power grids and delivering electricity to consumers. Currently, two primary technologies are employed for grid connection: three-phase high-voltage alternating current (HVAC) and high-voltage direct current (HVDC). Typically, HVAC is favored for short distances, whereas HVDC is preferred for long connections [3], [4]. This preference is partly due to the need for reactive compensation, required to address the charging currents induced by the high capacitance of submarine cables, and partly due to the low short-circuit ratio at the wind turbines' (WTs') terminals, resulting from the cable's high impedance. Modern WTs are conventionally controlled using grid-following (GFL) strategies, which means that their operation can be negatively affected under weak grid conditions [5]. Additionally, interactions between the WTs and the shunt inductors, commonly used for reactive power compensation, can lead to undesirable resonances, posing challenges for stable system operation and power quality at the grid connection point [6], [7]. This limits the feasible length of HVAC connections for offshore WPPs.

The solution lies in the installation of a static synchronous compensator (STATCOM) at the onshore grid-connection point (point of common coupling, PCC) of the WPP. This approach has been proven to enhance system stability and power quality, thus enabling the utilization of HVAC connections over longer distances [8]–[10]. Notable examples of HVAC-connected offshore wind farms include Hornsea One and Two in the UK, located 120 km and 90 km offshore, respectively [11], as well as Kriegers Flak in Denmark [12]. As the share of renewable energy generation in the power grid increases, grid codes are updated with requirements to provide some of the beneficial functionalities of synchronous generators (SGs), including fast fault-current injection, frequency support, inertial response, and black start capability [13]. This set of requirements is commonly referred to as grid-forming (GFM) capabilities, and they are seen as essential for further increasing the penetration of converter-based resources [14], [15]. The integration of energy storage systems with the STATCOM, often referred to as ES-STATCOM, enables the provision of active-power-based functionalities such as the inertial response and power oscillation damping from the STATCOM [16]. As

Submitted to the 23rd Power Systems Computation Conference (PSCC 2024).

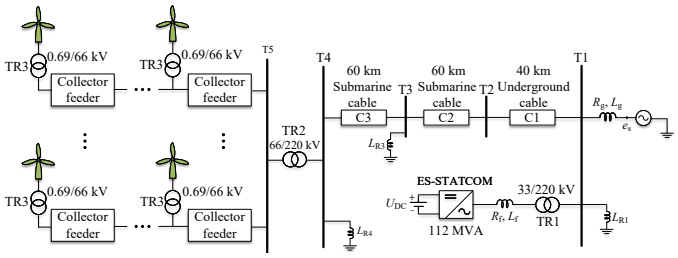

Fig. 1. Single-line diagram of the considered WPP.

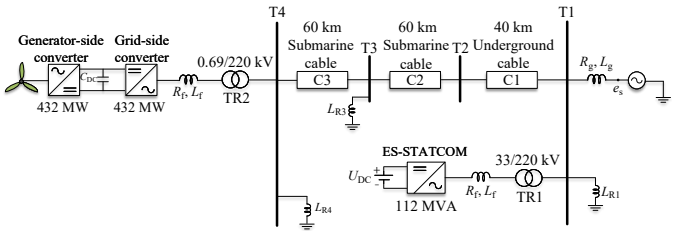

Fig. 2. Simplified model of the considered WPP.

outlined in [15], future converter-dominated grids will likely comprise a mix of both GFM and GFL converters, and recent studies suggest that a combination of both control modes might outperform a pure GFM setup [17].

This brings us to two central research questions that this paper aims to address. Firstly, which control mode for the STATCOM provides the most substantial stability margin for the WPP? Secondly, does the system with GFL-controlled WTs and GFM-controlled STATCOM provide GFM capabilities at the PCC? To answer these questions, the paper is structured as follows: Section II introduces the HVAC-connected offshore WPP with an onshore ES-STATCOM. Section III provides a detailed description of the controller design and small-signal modeling of the overall system, including controller specifics. In Section IV, the stability margin of the system is compared for GFL and GFM control modes in the ES-STATCOM using the generalized Nyquist criterion (GNC). To investigate the provision of GFM capabilities at the PCC, Section V presents and applies the method of network-frequency perturbation (NFP) plots to the examined system. Finally, the conclusions of the paper are given in Section VI.

II. Description of the WPP

The analyzed WPP is inspired by the Hornsea Two offshore WPP [18]–[20]. In this paper, only a portion of the offshore network is modelled in detail, as illustrated by the single-line diagram in Fig. 1. The considered plant comprises full-power converter WTs (Type-4), each rated at $8\,\mathrm{MW}$, $0.69/66\,\mathrm{kV}$, and operating at a power factor of 0.9. Multiple WTs are connected in various radials, which are then linked together at the AC-collection bus T5 to form the 432 MW wind farm. The entire wind farm is connected via a $66/220\,\mathrm{kV}$ transformer to the offshore substation, which serves as the offshore terminal T4 of the HVAC $220\,\mathrm{kV}$ transmission network. This network consists of two $60\,\mathrm{km}$ submarine cable sections (C2 and C3) and a $40\,\mathrm{km}$ onshore underground cable (C1). To accurately capture dynamics and multiple resonances, the $220\,\mathrm{kV}$ export cables are modeled utilizing the PSCAD cable modeling toolbox, incorporating cable parameters supplied by industrial partners. Reactive power compensation for the export cable network is facilitated by the installation of shunt reactors at various locations along the HVAC-transmission system. The sizing and location of these reactors are based on an actual case study conducted together with the industrial partners and using the analysis presented in [21]. Consequently, shunt reactors of 120 MVAr, 170 MVAr, and 90 MVAr are positioned at buses T1, T3, and T4, respectively. Furthermore, a 112 MVA ES-STATCOM is interconnected via a 112 MVA, $33/220\,\mathrm{kV}$ step-up transformer to the onshore terminal T1 to enhance stability, improve power quality, and provide voltage regulation. To enable active-power-based functionalities such as inertial response and power oscillation damping from the ES-STATCOM, typically, an energy storage device, such as a supercapacitor with limited storage capacity, is installed at the DC side. However, since the primary focus is not on evaluating the impact of the energy storage technology, an ideal-voltage source is assumed at the DC side of the ES-STATCOM, as illustrated in Fig. 1. Lastly, the onshore AC transmission grid is represented by its Thévenin equivalent, composed of a 220 kV ideal-voltage source situated behind a grid impedance. The grid impedance is adjusted based on the specific grid strength under investigation. Additional system parameters can be found in [22]. In this paper, the entire system encompassing all components from the WTs to bus T1 is referred to as the WPP.

As a trade-off between the complexity of the derived mathematical model for small-signal analysis and its accuracy, simplifications are made to the offshore network of the considered WPP from its practical configuration. Considering that one of the main objectives of the small-signal analysis performed in this study is to assess harmonic interactions between the WPP and the onshore AC transmission grid, the control interactions among WTs are disregarded. Instead, the WTs are collectively depicted as an aggregated 432 MW converter system, as shown in Fig. 2. Additionally, collector feeders linking the WTs to the 66 kV offshore substation are omitted. Instead, the WTs are directly linked via a $0.69/220\,\mathrm{kV}$ transformer to the offshore terminal T4, as illustrated in Fig. 2. Nevertheless, in order to verify the accuracy of the small-signal model derived from the simplified system, detailed time-domain simulations are performed. In these simulations, the number of radial connections within the offshore wind farm is limited to three due to constraints on the number of electrical nodes in the utilized simulation software. The findings of these simulations are then outlined in section IV.

III. Controller Design and System Modeling

In this section, a description of the different control structures governing the operation of both the WTs and the ES-

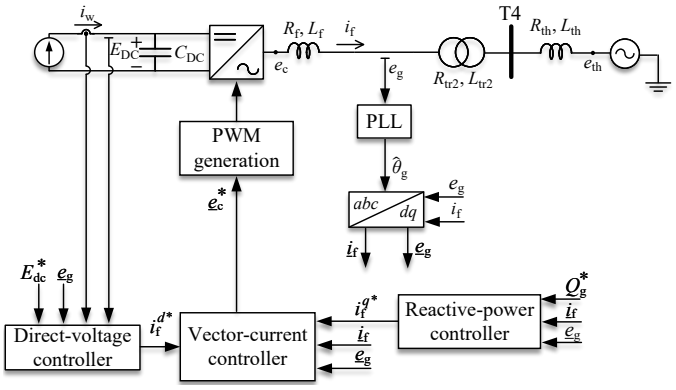

Fig. 3. WT main circuit diagram and control system.

STATCOM is provided. Additionally, frequency-dependent AC-side input admittance/impedance models are derived to facilitate the analysis of closed-loop stability for the entire wind power plant (WPP).

A. Description and Admittance Model of the Wind Turbine

The WT system considered here is constituted by a rotating machine connected to the offshore grid through a back-to-back converter as illustrated in Fig. 2. As the dc-link of the back-to-back converter decouples the machine-side ac system from the grid under normal system operations, the equivalent circuit in Fig. 3 can be employed for analysis purpose, where a variable current source is used to represent the machine side and the rectifier stage of the WT [23]. The rest of the system to the right side of the offshore terminal T4 is represented by its Thévenin equivalent in Fig. 3. The main control loops of the WT as shown in Fig. 3 are implemented in the rotating *dq*-reference frame (using power-invariant transformation), which is defined using the estimated grid-voltage angle obtained from the PLL, $\hat{\theta}_{\rm g}$, and is aligned with the measured grid-voltage vector. Therefore, the estimated angle from the PLL is given by

$$\hat{\theta}_{\rm g} = \overbrace{\frac{1}{s}(K_{\rm p,PLL} + \frac{K_{\rm i,PLL}}{s})}^{F_{\rm PLL}} \tan^{-1}(\frac{e_{\rm g}^q}{e_{\rm g}^d}) + \frac{\omega_{\rm N}}{s}, \qquad (1)$$

where $K_{\rm p,PLL}$ and $K_{\rm i,PLL}$ represent the proportional and integral gains of the PLL, respectively. The term s is the Laplace-transform variable, which should be interpreted as d/dt wherever appropriate. With $\alpha_{\rm PLL}$ denoting the loop bandwidth of the synchronization algorithm, these gains are selected as $K_{\rm p,PLL} = 2\alpha_{\rm PLL}$ and $K_{\rm i,PLL} = \alpha_{\rm PLL}^2$ [23].

As shown in Fig. 3, the control algorithm for WT has a cascade structure, with an inner ac-current controller and two outer-loop controllers, namely, the reactive-power controller and dc-voltage controller. The reactive-power and dc-voltage controllers generate the reference reactive- and active-current components, respectively, for the inner vector-current controller that calculates the converter voltage reference, $\underline{e}_{\rm c}^{\star}$, for the modulation stage of the converter. The implemented current controller has a classical structure and is based on a PI regulator with cross-coupling cancellation and voltage feed-forward that is low-pass filtered with a closed-loop bandwidth of $\alpha_{\rm ff}$. The current controller calculates the converter-voltage reference as

$$\underline{e}_{\rm c}^{\star} = \overbrace{\frac{\alpha_{\rm ff}}{s+\alpha_{\rm ff}}}^{H_{\rm ff}} \underline{e}_{\rm g} + j\omega_{\rm N} L_{\rm f} \underline{i}_{\rm f} + \overbrace{(K_{\rm p,cc} + \frac{K_{\rm i,cc}}{s})}^{G_{\rm cc}} (\underline{i}_{\rm f}^{\star} - \underline{i}_{\rm f}). \quad (2)$$

$K_{\rm p,cc}$, $K_{\rm i,cc}$ denote the proportional and integral gains of the PI regulator for the current controller, respectively, and "$\star$" denotes a reference signal in the notations. These gains are calculated using the classical loop-shaping approach as $K_{\rm p,cc} = \alpha_{\rm cc} L_{\rm f}$ and $K_{\rm i,cc} = \alpha_{\rm cc} R_{\rm f}$, where $\alpha_{\rm cc}$ denotes the loop bandwidth of the current controller [23].

The reactive-power controller is used to regulate the reactive power, $Q_{\rm g}$, injected by the WT to the grid. It calculates the reference reactive-current component, $i_{\rm f}^{q\star}$, as

$$i_{\rm f}^{q\star} = G_{\rm qc} \frac{(Q_{\rm g}^{\star} - Q_{\rm g})}{E_{\rm N}}; \quad G_{\rm qc} = \frac{K_{\rm i,qc}}{s}, \qquad (3)$$

where $Q_{\rm g}^{\star}$ denotes the reference reactive power and $E_{\rm N}$ is the rated line-to-line voltage of the converter. With $\alpha_{\rm qc}$ denoting the closed-loop bandwidth of the reactive-power controller, the integral gain is selected using the loop-shaping approach as $K_{\rm i,qc} = -\alpha_{\rm qc}$ [23].

The dc-voltage controller is used to regulate the direct voltage, $E_{\rm dc}$, of the converter, which is measured across the dc capacitance, $C_{\rm dc}$. It calculates the reference active-current component, $i_{\rm f}^{d\star}$, as [23]

$$i_{\rm f}^{d\star} = \frac{K_{\rm p,dc}(E_{\rm dc}^{\star 2}/2 - E_{\rm dc}^2/2) + H_{\rm dc} P_{\rm w}}{E_{\rm g}}, \qquad (4)$$

where $E_{\rm dc}^{\star}$ is the reference dc voltage of the converter and $E_{\rm g}$ denotes the magnitude of the grid voltage. The power from the machine-side converter in the WT, $P_{\rm w} = E_{\rm dc} I_{\rm w}$ (see Fig. 3), is filtered using a low-pass filter represented by the transfer function $H_{\rm dc}$ and added as a feed-forward term in (4) to enhance the system dynamics. With $\alpha_{\rm dc}$ denoting the closed-loop bandwidth of the dc-voltage controller, the proportional gain is selected as $K_{\rm p,dc} = -\alpha_{\rm dc} C_{\rm dc}$ [23]. Neglecting the converter losses, the dc-link voltage dynamics can be expressed as

$$\frac{C_{\rm dc}}{2} \frac{dE_{\rm dc}^2}{dt} = P_{\rm w} - P_{\rm conv}, \qquad (5)$$

where $P_{\rm conv}$ denotes the converter output active power at its ac-side terminal.

In order to account for the dynamics of the PLL in the system model, the input admittance of the converter is derived in the *dq*-frame, which is defined by the angle $\theta_{\rm N}$, obtained by integrating the rated angular frequency, $\omega_{\rm N}$, and having a zero initial phase. For this, the controller dynamics described above should be transformed to this frame (referred here as

source dq-frame). It can be observed from (1) that the angle θ_{N} is given by

$$\theta_{\mathrm{N}} = \hat{\theta}_{\mathrm{g}} - \theta_{\mathrm{L}}, \quad \text{with} \quad \theta_{\mathrm{L}} = F_{\mathrm{PLL}} \tan^{-1}\left(\frac{e^q_{\mathrm{g}}}{e^d_{\mathrm{g}}}\right), \tag{6}$$

where θ_{L} represents the angle difference between the *converter dq-frame* (defined by the PLL) and *source dq-frame*. Thus, any space-vector $\underline{y}$ defined earlier can be transformed to the *source dq-frame* using the following relation

$$\underline{y}^s = \underline{y} e^{j\theta_{\mathrm{L}}}, \tag{7}$$

where the superscript *s* is used to represent entities in the *source dq-frame*.

In order to derive the input admittance, the small-signal models of grid-voltage, converter current and converter-voltage reference can be transformed from *converter dq-frame* to *source dq-frame* and expressed in scalar form using (1), (6) and (7) as

$$\begin{bmatrix}\Delta e_{\mathrm{g,d}} \\ \Delta e_{\mathrm{g,q}}\end{bmatrix} = \overbrace{\begin{bmatrix}\cos\theta_{\mathrm{L0}} & \sin\theta_{\mathrm{L0}} \\ -\sin\theta_{\mathrm{L0}} & \cos\theta_{\mathrm{L0}}\end{bmatrix}}^{\mathbf{G}_{\mathrm{Tx}}} \begin{bmatrix}\Delta e^s_{\mathrm{g,d}} \\ \Delta e^s_{\mathrm{g,q}}\end{bmatrix} + \overbrace{G_{\mathrm{PLL}} \begin{bmatrix}A_{\mathrm{e}} & B_{\mathrm{e}} \\ E_{\mathrm{g0}}\sin\theta_{\mathrm{L0}} & -E_{\mathrm{g0}}\cos\theta_{\mathrm{L0}}\end{bmatrix}}^{\mathbf{G}_{\mathrm{e,PLL}}} \begin{bmatrix}\Delta e^s_{\mathrm{g,d}} \\ \Delta e^s_{\mathrm{g,q}}\end{bmatrix}, \tag{8}$$

$$\begin{bmatrix}\Delta i_{\mathrm{f,d}} \\ \Delta i_{\mathrm{f,q}}\end{bmatrix} = \mathbf{G}_{\mathrm{Tx}} \begin{bmatrix}\Delta i^s_{\mathrm{f,d}} \\ \Delta i^s_{\mathrm{f,q}}\end{bmatrix} + \overbrace{G_{\mathrm{PLL}} \begin{bmatrix}A_{\mathrm{i}} & B_{\mathrm{i}} \\ I_{\mathrm{f0}}\sin\theta_{\mathrm{L0}} & -I_{\mathrm{f0}}\cos\theta_{\mathrm{L0}}\end{bmatrix}}^{\mathbf{G}_{\mathrm{i,PLL}}} \begin{bmatrix}\Delta e^s_{\mathrm{g,d}} \\ \Delta e^s_{\mathrm{g,q}}\end{bmatrix}, \tag{9}$$

$$\begin{bmatrix}\Delta e^{\star}_{\mathrm{c,d}} \\ \Delta e^{\star}_{\mathrm{c,q}}\end{bmatrix} = \mathbf{G}_{\mathrm{Tx}} \begin{bmatrix}\Delta e^{s\star}_{\mathrm{c,d}} \\ \Delta e^{s\star}_{\mathrm{c,q}}\end{bmatrix} + \overbrace{G_{\mathrm{PLL}} \begin{bmatrix}A_{\mathrm{d}} & B_{\mathrm{d}} \\ E_{\mathrm{c0}}\sin\theta_{\mathrm{L0}} & -E_{\mathrm{c0}}\cos\theta_{\mathrm{L0}}\end{bmatrix}}^{\mathbf{G}_{\mathrm{d,PLL}}} \begin{bmatrix}\Delta e^s_{\mathrm{g,d}} \\ \Delta e^s_{\mathrm{g,q}}\end{bmatrix}. \tag{10}$$

The expressions for G_{PLL}, A_{e}, B_{e}, E_{g0}, A_{i}, B_{i}, I_{f0}, A_{d}, B_{d}, and E_{c0} are provided in the appendix. Note that "Δ" denotes small-signal perturbations around the steady-state quantities represented by the subscript "0" in the notations.

The small-signal model of the converter-voltage reference can be expressed in its scalar form using (2) as

$$\begin{bmatrix}\Delta e^{\star}_{\mathrm{c,d}} \\ \Delta e^{\star}_{\mathrm{c,q}}\end{bmatrix} = \overbrace{\begin{bmatrix}H_{\mathrm{ff}} & 0 \\ 0 & H_{\mathrm{ff}}\end{bmatrix}}^{\mathbf{G}_{\mathrm{ff}}} \begin{bmatrix}\Delta e_{\mathrm{g,d}} \\ \Delta e_{\mathrm{g,q}}\end{bmatrix} + \overbrace{\begin{bmatrix}G_{\mathrm{cc}} & 0 \\ 0 & G_{\mathrm{cc}}\end{bmatrix}}^{\mathbf{G}_{\mathrm{c}}} \begin{bmatrix}\Delta i^{\star}_{\mathrm{f,d}} \\ \Delta i^{\star}_{\mathrm{f,q}}\end{bmatrix} + \overbrace{\begin{bmatrix}-G_{\mathrm{cc}} & -\omega_{\mathrm{N}} L_{\mathrm{f}} \\ \omega_{\mathrm{N}} L_{\mathrm{f}} & -G_{\mathrm{cc}}\end{bmatrix}}^{\mathbf{Y}_{\mathrm{i}}} \begin{bmatrix}\Delta i_{\mathrm{f,d}} \\ \Delta i_{\mathrm{f,q}}\end{bmatrix}. \tag{11}$$

By using the expressions (8)-(11) the small-signal model of the converter-voltage reference can be expressed in the *source dq-frame* as

$$\begin{aligned}\begin{bmatrix}\Delta e^{s\star}_{\mathrm{c,d}} \\ \Delta e^{s\star}_{\mathrm{c,q}}\end{bmatrix} &= \mathbf{G}^{-1}_{\mathrm{Tx}}\mathbf{G}_{\mathrm{ff}}(\mathbf{G}_{\mathrm{Tx}} + \mathbf{G}_{\mathrm{e,PLL}}) \begin{bmatrix}\Delta e^s_{\mathrm{g,d}} \\ \Delta e^s_{\mathrm{g,q}}\end{bmatrix} \\ &+ \mathbf{G}^{-1}_{\mathrm{Tx}}\mathbf{G}_{\mathrm{c}} \begin{bmatrix}\Delta i^{\star}_{\mathrm{f,d}} \\ \Delta i^{\star}_{\mathrm{f,q}}\end{bmatrix} + \mathbf{G}^{-1}_{\mathrm{Tx}}\mathbf{Y}_{\mathrm{i}}\mathbf{G}_{\mathrm{Tx}} \begin{bmatrix}\Delta i^s_{\mathrm{f,d}} \\ \Delta i^s_{\mathrm{f,q}}\end{bmatrix} \\ &+ \mathbf{G}^{-1}_{\mathrm{Tx}}\mathbf{Y}_{\mathrm{i}}\mathbf{G}_{\mathrm{i,PLL}} \begin{bmatrix}\Delta e^s_{\mathrm{g,d}} \\ \Delta e^s_{\mathrm{g,q}}\end{bmatrix} - \mathbf{G}^{-1}_{\mathrm{Tx}}\mathbf{G}_{\mathrm{d,PLL}} \begin{bmatrix}\Delta e^s_{\mathrm{g,d}} \\ \Delta e^s_{\mathrm{g,q}}\end{bmatrix}.\end{aligned} \tag{12}$$

The small-signal model of the converter output voltage in the *source dq-frame* can be expressed in scalar form as

$$\begin{bmatrix}\Delta e^s_{\mathrm{c,d}} \\ \Delta e^s_{\mathrm{c,q}}\end{bmatrix} = I \begin{bmatrix}\Delta e^s_{\mathrm{g,d}} \\ \Delta e^s_{\mathrm{g,q}}\end{bmatrix} + \overbrace{\begin{bmatrix}R_{\mathrm{f}} + sL_{\mathrm{f}} & -\omega_{\mathrm{N}} L_{\mathrm{f}} \\ \omega_{\mathrm{N}} L_{\mathrm{f}} & R_{\mathrm{f}} + sL_{\mathrm{f}}\end{bmatrix}}^{\mathbf{Z}_{\mathrm{f}}} \begin{bmatrix}\Delta i^s_{\mathrm{f,d}} \\ \Delta i^s_{\mathrm{f,q}}\end{bmatrix}, \tag{13}$$

where I denotes the identity matrix. Using the expressions for the reactive power injected into the grid, $Q_{\mathrm{g}} = -e^s_{\mathrm{g,d}} i^s_{\mathrm{f,q}} + e^s_{\mathrm{g,q}} i^s_{\mathrm{f,d}}$, the converter output active power, $P_{\mathrm{conv}} = e^s_{\mathrm{c,d}} i^s_{\mathrm{f,d}} + e^s_{\mathrm{c,q}} i^s_{\mathrm{f,q}}$, grid-voltage magnitude, $E_{\mathrm{g}} = \sqrt{(e^s_{\mathrm{g,d}})^2 + (e^s_{\mathrm{g,q}})^2}$, and converter output voltage in (13), the small-signal model of the reference active- and reactive-current components can be obtained from (3)-(5) and (13) as

$$\begin{bmatrix}\Delta i^{\star}_{\mathrm{f,d}} \\ \Delta i^{\star}_{\mathrm{f,q}}\end{bmatrix} = \mathbf{F}_{\mathrm{Qdc}} \begin{bmatrix}\Delta E^{\star}_{\mathrm{dc}} \\ \Delta Q^{\star}_{\mathrm{g}} \\ \Delta P_{\mathrm{w}}\end{bmatrix} + \mathbf{G}_{\mathrm{Qdc}} \begin{bmatrix}\Delta i^s_{\mathrm{f,d}} \\ \Delta i^s_{\mathrm{f,q}}\end{bmatrix} + \mathbf{Y}_{\mathrm{Qdc}} \begin{bmatrix}\Delta e^s_{\mathrm{g,d}} \\ \Delta e^s_{\mathrm{g,q}}\end{bmatrix}, \tag{14}$$

where the power generated from the wind turbine is considered as an input in (14). The expressions for the transfer matrices $\mathbf{G}_{\mathrm{Qdc}}$ and $\mathbf{Y}_{\mathrm{Qdc}}$ are provided in the appendix. However, since the transfer matrix $\mathbf{F}_{\mathrm{Qdc}}$ is not utilized further in the analysis, its expression is not included in the manuscript.

Since one of the objectives of the study conducted here is to examine the grid-forming properties of the WPP, which are typically defined in the subsynchronous frequency range (where the PLL and outer-power controllers are predominantly active), the influence of delays resulting from the discretization of measured quantities and those arising from the modulation stage are disregarded in the derived small-signal models. Consequently, the small-signal model of the converter output voltage can be equated to that of its reference, i.e.,

$$\begin{bmatrix}\Delta e^s_{\mathrm{c,d}} \\ \Delta e^s_{\mathrm{c,q}}\end{bmatrix} = \begin{bmatrix}\Delta e^{s\star}_{\mathrm{c,d}} \\ \Delta e^{s\star}_{\mathrm{c,q}}\end{bmatrix}. \tag{15}$$

Finally, by using expressions in (12)-(15), the input admittance of the WT, $\mathbf{Y}_{\mathrm{WT}}$, in the *source dq-frame* is derived as[1]

$$\begin{bmatrix}\Delta i^s_{\mathrm{f,d}} \\ \Delta i^s_{\mathrm{f,q}}\end{bmatrix} = \mathbf{G}_{\mathrm{WT}} \begin{bmatrix}\Delta E^{\star}_{\mathrm{dc}} \\ \Delta Q^{\star}_{\mathrm{q}} \\ \Delta P_{\mathrm{w}}\end{bmatrix} - \mathbf{Y}_{\mathrm{WT}} \begin{bmatrix}\Delta e^s_{\mathrm{g,d}} \\ \Delta e^s_{\mathrm{g,q}}\end{bmatrix}, \tag{16}$$

[1]Since the direction of current flowing out of the converter in Fig. 3 is taken as positive, the negative sign for $\mathbf{Y}_{\mathrm{WT}}$ is used in (16).

where $\mathbf{Y}_{\mathrm{WT}}$ is given by

$$\begin{aligned}\mathbf{Y}_{\mathrm{WT}} =&[\mathbf{G}_{\mathrm{Tx}}^{-1}\mathbf{Y}_{\mathrm{i}}\mathbf{G}_{\mathrm{Tx}} + \mathbf{G}_{\mathrm{Tx}}^{-1}\mathbf{G}_{\mathrm{c}}\mathbf{G}_{\mathrm{Qdc}} - \mathbf{Z}_{\mathrm{f}}]^{-1} \\ &[\mathbf{G}_{\mathrm{Tx}}^{-1}\mathbf{G}_{\mathrm{ff}}(\mathbf{G}_{\mathrm{Tx}} + \mathbf{G}_{\mathrm{e,PLL}}) + \mathbf{G}_{\mathrm{Tx}}^{-1}\mathbf{Y}_{\mathrm{i}}\mathbf{G}_{\mathrm{i,PLL}} \\ &- \mathbf{G}_{\mathrm{Tx}}^{-1}\mathbf{G}_{\mathrm{d,PLL}} + \mathbf{G}_{\mathrm{Tx}}^{-1}\mathbf{G}_{\mathrm{c}}\mathbf{Y}_{\mathrm{Qdc}} - I]\end{aligned}$$

B. Description and Admittance Model of the ES-STATCOM

1) ES-STATCOM operated in GFM mode: Figure 4 shows the single-line diagram of the considered ES-STATCOM together with a block-scheme of the implemented GFM control. Given its high-power and high-voltage nature, the double-Y modular multilevel converter topology is frequently employed for STATCOM applications [24]. However, since this study primarily concerns the system dynamics in the subsynchronous frequency range, the specific topology of the converter itself does not significantly influence the outcomes. Consequently, an average model of the converter is utilized to represent the ES-STATCOM.

The GFM control adopted in this work for the ES-STATCOM is based on the direct control of converter voltage (DCCV) approach from [22]. In this type of control strategy, the ac-voltage controller typically regulates the magnitude of the voltage at the PCC and calculates the reference value of the converter-voltage magnitude, $E_{\mathrm{c}}^{\star}$; whereas, the active-power controller calculates the converter-voltage angle, θ_{c}. If necessary, a droop-based frequency-control loop can be incorporated in cascade with the active-power controller to regulate the frequency and calculate the reference for the active power, $P_{\mathrm{g}}^{\star}$. However, given the assumption of limited energy storage for the ES-STATCOM, this loop is disregarded. All controllers described here are designed in the converter *dq*-reference frame (using power-invariant transformation), which is defined by the angle output of the active-power controller.

To facilitate fault-ride-through operation of the ES-STATCOM, an embedded current controller is employed with this specific control strategy [25]. This controller is triggered only when the converter current surpasses its maximum allowable value, particularly during fault conditions. In normal operation, which is the criteria for conducting small-signal analysis, the current controller remains inactive and does not affect the system [25]. Therefore, it is omitted from the block diagram of the DCCV shown in Fig. 4, and it is not considered in the derivation of the linearized model of the ES-STATCOM.

The ac-voltage controller implemented here comprises of a pure integrator. Accordingly, the converter voltage reference, $\underline{e}_{\mathrm{c}}^{\star}$, is calculated as [22]

$$\underline{e}_{\mathrm{c}}^{\star} = E_{\mathrm{N}} + \overbrace{\frac{K_{\mathrm{i,vc}}}{s}}^{G'_{\mathrm{vc}}}\left(E_{\mathrm{g}}^{\star} - \overbrace{\frac{\alpha_{\mathrm{fmv}}}{s+\alpha_{\mathrm{fmv}}}}^{H_{\mathrm{fmv}}} E_{\mathrm{g}}\right) - \overbrace{\frac{s}{s+\alpha_{\mathrm{hpf}}}}^{G_{\mathrm{hpf}}} R'_{\mathrm{a}}\underline{i}_{\mathrm{f}}. \tag{17}$$

The term α_{fmv} denotes the cut-off frequency of the low-pass filter for the capacitor voltage measurement. A transient damping term comprising of high-pass filtered converter current is added at the output of the ac-voltage controller to prevent a poorly damped closed-loop system. R'_{a} denotes the

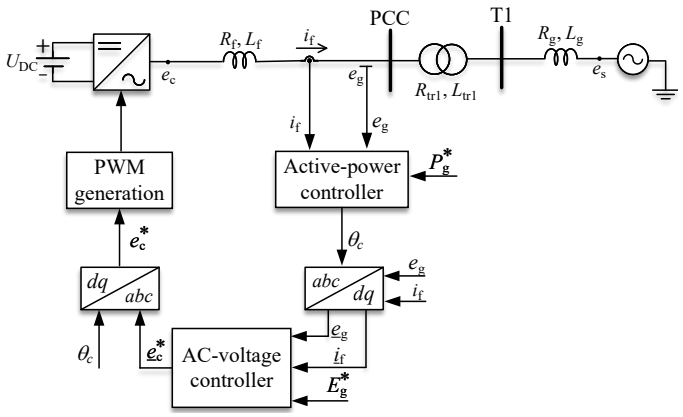

Fig. 4. Single-line diagram of the ES-STATCOM and block scheme of DCCV.

active resistance and α_{hpf} the cut-off frequency of the high-pass filter, whose values are selected as suggested in [22]. The integral gain of the controller, $K_{\mathrm{i,vc}}$, can be calculated using the loop-shaping approach as, $K_{\mathrm{i,vc}} = \frac{\alpha_{\mathrm{vc}}(X_{\mathrm{f}}+X_{\mathrm{tr1}}+\hat{X}_{\mathrm{g}})}{(X_{\mathrm{tr1}}+\hat{X}_{\mathrm{g}})}$, where α_{vc} denotes the desired closed-loop bandwidth. X in the notations denote the reactance of the corresponding inductance. In order to guarantee the desired speed of response for all grid conditions, $\hat{X}_{\mathrm{g}}$ is typically set for the strongest grid strength provided by the system operator [22].

The active-power controller calculates the converter-voltage angle as [22]

$$\theta_{\mathrm{c}} = \frac{1}{s}\overbrace{[(K_{\mathrm{p,pc}} + \frac{K_{\mathrm{i,pc}}}{s})}^{G_{\mathrm{pc}}}\frac{(P_{\mathrm{g}}^{\star} - P_{\mathrm{g}})}{S_{\mathrm{N}}} - R_{\mathrm{a}}\frac{P_{\mathrm{g}}}{S_{\mathrm{N}}} + \omega_{\mathrm{N}}], \tag{18}$$

The parameters of the active-power controller are tuned to obtain a first-order closed-loop response from $P_{\mathrm{g}}^{\star}$ to P_{g} [22]. Accordingly, $K_{\mathrm{p,pc}} = \frac{\alpha_{\mathrm{pc}}}{K_{\mathrm{s}}}S_{\mathrm{N}}, K_{\mathrm{i,pc}} = \frac{\alpha_{\mathrm{pc}}^2}{K_{\mathrm{s}}}S_{\mathrm{N}}$ and $R_{\mathrm{a}} = K_{\mathrm{p,pc}}$, with α_{pc} the loop bandwidth (in rad/s) of the active-power controller and synchronizing power coefficient given by $K_{\mathrm{s}} = \frac{E_{\mathrm{c}}E_{\mathrm{s}}}{(X_{\mathrm{f}}+X_{\mathrm{tr1}}+\hat{X}_{\mathrm{g}})}$.

In order to account for the dynamics of the active-power controller in the system model, the input admittance of the converter is derived in the *source dq-frame*. For this, the controller dynamics described above should be transformed to this frame. It can be observed from (18) that the angle θ_{N} is given by

$$\theta_{\mathrm{N}} = \theta_{\mathrm{g}} - \theta_{\mathrm{L}}, \quad \text{with} \quad \theta_{\mathrm{L}} = \frac{1}{s}\frac{[G_{\mathrm{pc}}(P_{\mathrm{g}}^{\star} - P_{\mathrm{g}}) - R_{\mathrm{a}}P_{\mathrm{g}}]}{S_{\mathrm{N}}}, \tag{19}$$

where θ_{L} represents the phase-angle difference between the converter-voltage and the ideal-voltage source, and can be interpreted as the converter's load angle. Thus, any space-vector $\underline{z}$ defined earlier can be transformed to the *source dq-frame* using the following relation

$$\underline{z}^{s} = \underline{z}e^{j\theta_{\mathrm{L}}}. \tag{20}$$

Using (17)-(20), the small-signal model of the converter-voltage reference in the *source dq-frame* can be expressed as

$$\begin{bmatrix}\Delta e^{s\star}_{\mathrm{c,d}}\\ \Delta e^{s\star}_{\mathrm{c,q}}\end{bmatrix} = \overbrace{\begin{bmatrix}-(e^s_{\mathrm{c,q0}}+G_{\mathrm{hpf}}R'_{\mathrm{a}}i^s_{\mathrm{f,q0}}) & G'_{\mathrm{vc}}\cos\theta_{\mathrm{L0}}\\ (e^s_{\mathrm{c,d0}}+G_{\mathrm{hpf}}R'_{\mathrm{a}}i^s_{\mathrm{f,d0}}) & G'_{\mathrm{vc}}\sin\theta_{\mathrm{L0}}\end{bmatrix}}^{\mathbf{G}'_{\mathrm{T}}}\begin{bmatrix}\Delta\theta_{\mathrm{L}}\\ \Delta E_{\mathrm{set}}\end{bmatrix}$$
$$+G'_{\mathrm{vc}}\left(-\overbrace{\begin{bmatrix}\frac{H_{\mathrm{fmv}}\cos\theta_{\mathrm{L0}}e^s_{\mathrm{g,d0}}}{E_{\mathrm{g0}}} & \frac{H_{\mathrm{fmv}}\cos\theta_{\mathrm{L0}}e^s_{\mathrm{g,q0}}}{E_{\mathrm{g0}}}\\ \frac{H_{\mathrm{fmv}}\sin\theta_{\mathrm{L0}}e^s_{\mathrm{g,d0}}}{E_{\mathrm{g0}}} & \frac{H_{\mathrm{fmv}}\sin\theta_{\mathrm{L0}}e^s_{\mathrm{g,q0}}}{E_{\mathrm{g0}}}\end{bmatrix}}^{\mathbf{G}'_{\mathrm{PVv1}}}\right)\begin{bmatrix}\Delta e^s_{\mathrm{g,d}}\\ \Delta e^s_{\mathrm{g,q}}\end{bmatrix}$$
$$+\overbrace{\begin{bmatrix}-G_{\mathrm{hpf}}R'_{\mathrm{a}} & 0\\ 0 & -G_{\mathrm{hpf}}R'_{\mathrm{a}}\end{bmatrix}}^{\mathbf{G}_{\mathrm{DH}}}\begin{bmatrix}\Delta i^s_{\mathrm{f,d}}\\ \Delta i^s_{\mathrm{f,q}}\end{bmatrix}, \tag{21}$$

with

$$\begin{bmatrix}\Delta\theta_{\mathrm{L}}\\ \Delta E_{\mathrm{set}}\end{bmatrix} = \begin{bmatrix}\frac{G_{\mathrm{pc}}}{sS_{\mathrm{N}}} & 0\\ 0 & 1\end{bmatrix}\begin{bmatrix}\Delta P^\star_{\mathrm{g}}\\ \Delta E_{\mathrm{set}}\end{bmatrix}$$
$$+\overbrace{\begin{bmatrix}-\frac{(G_{\mathrm{pc}}+R_{\mathrm{a}})e^s_{\mathrm{g,d0}}}{sS_{\mathrm{N}}} & -\frac{(G_{\mathrm{pc}}+R_{\mathrm{a}})e^s_{\mathrm{g,q0}}}{sS_{\mathrm{N}}}\\ 0 & 0\end{bmatrix}}^{\mathbf{G}_{\mathrm{PVc2}}}\begin{bmatrix}\Delta i^s_{\mathrm{f,d}}\\ \Delta i^s_{\mathrm{f,q}}\end{bmatrix}$$
$$+\overbrace{\begin{bmatrix}-\frac{(G_{\mathrm{pc}}+R_{\mathrm{a}})i^s_{\mathrm{f,d0}}}{sS_{\mathrm{N}}} & -\frac{(G_{\mathrm{pc}}+R_{\mathrm{a}})i^s_{\mathrm{f,q0}}}{sS_{\mathrm{N}}}\\ 0 & 0\end{bmatrix}}^{\mathbf{G}_{\mathrm{PVv2}}}\begin{bmatrix}\Delta e^s_{\mathrm{g,d}}\\ \Delta e^s_{\mathrm{g,q}}\end{bmatrix}, \tag{22}$$

where the expression $P_{\mathrm{g}} = e^s_{\mathrm{g,d}}i^s_{\mathrm{f,d}} + e^s_{\mathrm{g,q}}i^s_{\mathrm{f,q}}$, and $E_{\mathrm{g}} = \sqrt{(e^s_{\mathrm{g,d}})^2+(e^s_{\mathrm{g,q}})^2}$ are used for the active power injected to the grid and PCC-voltage magnitude, respectively. Now by neglecting the impact of delays and utilizing the small-signal model for the current dynamics in the *source dq-frame*, which is given by

$$\underline{e}^s_{\mathrm{c}} = \underline{e}^s_{\mathrm{g}} + j\omega_{\mathrm{N}}L_{\mathrm{f}}\underline{i}^s_{\mathrm{f}} + R_{\mathrm{f}}\underline{i}^s_{\mathrm{f}} + sL_{\mathrm{f}}\underline{i}^s_{\mathrm{f}}, \tag{23}$$

the input admittance of the ES-STATCOM in GFM mode is derived as

$$\begin{aligned}\mathbf{Y}_{\mathrm{GFM}} = &[\mathbf{G}'_{\mathrm{T}}\mathbf{G}_{\mathrm{PVc2}} + \mathbf{G}_{\mathrm{DH}} - \mathbf{Z}_{\mathrm{f}}]^{-1}\\ &[\mathbf{G}'_{\mathrm{T}}\mathbf{G}_{\mathrm{PVv2}} - G'_{\mathrm{vc}}\mathbf{G}'_{\mathrm{PVv1}} - I],\end{aligned} \tag{24}$$

$$\text{with}\quad \mathbf{Z}_{\mathrm{f}} = \begin{bmatrix}R_{\mathrm{f}}+sL_{\mathrm{f}} & -\omega_{\mathrm{N}}L_{\mathrm{f}}\\ \omega_{\mathrm{N}}L_{\mathrm{f}} & R_{\mathrm{f}}+sL_{\mathrm{f}}\end{bmatrix}.$$

2) ES-STATCOM operated in GFL mode: When the ES-STATCOM is operated in GFL mode instead, a similar control structure to the one described for WTs is implemented, with the only difference lying in the outer control loops. In this case, the active-power controller calculates the active-current component as

$$i^{d\star}_{\mathrm{f}} = G_{\mathrm{pc}}\frac{(P^\star_{\mathrm{g}} - P_{\mathrm{g}})}{E_{\mathrm{N}}};\quad G_{\mathrm{pc}} = \frac{K_{\mathrm{i,pc}}}{s}. \tag{25}$$

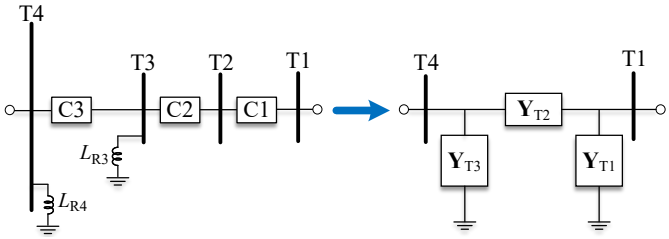

Fig. 5. Black-box modeling of the HVAC transmission network.

The integral gain is selected as $K_{\mathrm{i,pc}} = \alpha_{\mathrm{pc}}$. On the other hand, the PCC-voltage controller calculates the reactive-current component as

$$i^{q\star}_{\mathrm{f}} = G_{\mathrm{vc}}(E^\star_{\mathrm{g}} - E_{\mathrm{g}});\quad G_{\mathrm{vc}} = \frac{K_{\mathrm{i,vc}}}{s}, \tag{26}$$

where the integral gain is selected as $K_{\mathrm{i,vc}} = \frac{-\alpha_{\mathrm{vc}}}{X_{\mathrm{tr1}}+\hat{X}_{\mathrm{g}}}$.

Accordingly, the small-signal model of the reference active- and reactive-current components can be obtained from (25) and (26) as

$$\begin{bmatrix}\Delta i^\star_{\mathrm{f,d}}\\ \Delta i^\star_{\mathrm{f,q}}\end{bmatrix} = \mathbf{F}_{\mathrm{PV}}\begin{bmatrix}\Delta P^\star_{\mathrm{g}}\\ \Delta E^\star_{\mathrm{g}}\end{bmatrix} + \mathbf{G}_{\mathrm{PV}}\begin{bmatrix}\Delta i^s_{\mathrm{f,d}}\\ \Delta i^s_{\mathrm{f,q}}\end{bmatrix} + \mathbf{Y}_{\mathrm{PV}}\begin{bmatrix}\Delta e^s_{\mathrm{g,d}}\\ \Delta e^s_{\mathrm{g,q}}\end{bmatrix}. \tag{27}$$

The expressions for the transfer matrices $\mathbf{G}_{\mathrm{PV}}$ and $\mathbf{Y}_{\mathrm{PV}}$ are provided in the appendix. However, since the transfer matrix $\mathbf{F}_{\mathrm{PV}}$ is not utilized further in the analysis, its expression is not included in the manuscript. By utilizing equations (12), (13), (27) and neglecting the impact of delays, the input admittance of the ES-STATCOM for this case is given by

$$\begin{aligned}\mathbf{Y}_{\mathrm{GFL}} = &[\mathbf{G}^{-1}_{\mathrm{Tx}}\mathbf{Y}_{\mathrm{i}}\mathbf{G}_{\mathrm{Tx}} + \mathbf{G}^{-1}_{\mathrm{Tx}}\mathbf{G}_{\mathrm{c}}\mathbf{G}_{\mathrm{PV}} - \mathbf{Z}_{\mathrm{f}}]^{-1}\\ &[\mathbf{G}^{-1}_{\mathrm{Tx}}\mathbf{G}_{\mathrm{ff}}(\mathbf{G}_{\mathrm{Tx}} + \mathbf{G}_{\mathrm{e,PLL}}) + \mathbf{G}^{-1}_{\mathrm{Tx}}\mathbf{Y}_{\mathrm{i}}\mathbf{G}_{\mathrm{i,PLL}}\\ &- \mathbf{G}^{-1}_{\mathrm{Tx}}\mathbf{G}_{\mathrm{d,PLL}} + \mathbf{G}^{-1}_{\mathrm{Tx}}\mathbf{G}_{\mathrm{c}}\mathbf{Y}_{\mathrm{PV}} - I].\end{aligned}$$

C. Impedance Model of the Transformers and Shunt Reactor

For simplicity, the transformers are modeled as their respective equivalent leakage inductance L_{trN} and resistance R_{trN} ($N \in \{1,2\}$). Thus in *dq*-frame, the impedance of transformers is given as

$$\mathbf{Z}_{\mathrm{trN}} = \begin{bmatrix}R_{\mathrm{trN}}+sL_{\mathrm{trN}} & -\omega_{\mathrm{N}}L_{\mathrm{trN}}\\ \omega_{\mathrm{N}}L_{\mathrm{trN}} & R_{\mathrm{trN}}+sL_{\mathrm{trN}}\end{bmatrix}. \tag{28}$$

The impedance model of the 120 MVAr shunt reactor at the terminal T1 in *dq*-frame is given by

$$\mathbf{Z}_{\mathrm{R1}} = \begin{bmatrix}sL_{\mathrm{R1}} & -\omega_{\mathrm{N}}L_{\mathrm{R1}}\\ \omega_{\mathrm{N}}L_{\mathrm{R1}} & sL_{\mathrm{R1}}\end{bmatrix}, \tag{29}$$

where L_{R1} denotes the inductance of the shunt reactor.

D. Admittance Model of the Transmission Network

To accurately capture the dynamics of the transmission network, a two-port black-box modeling approach is employed in this study, as illustrated in Fig. 5. The admittance matrix of the two-port network from terminal T4 to T1 is obtained by conducting frequency scans in PSCAD at terminals T1 and T4. The methodology outlined in [26] is adopted to extract the elements of the admittance matrix from the simulation model.

To conduct the frequency scan at terminal T1, a voltage source is connected to terminal T1 while terminal T4 is grounded. The *dq*-components of the source voltage are independently perturbed at various frequencies ranging from 1 Hz to 1 kHz. For each perturbation, the resulting perturbations in the *dq*-components of the currents at the two ports are measured, and the elements of the admittance matrix of the two-port network are extracted using Discrete Fourier Transform (DFT) calculations. Similarly, to perform the frequency scan at terminal T4, a voltage source is connected to terminal T4 while terminal T1 is grounded, and the aforementioned process is repeated.

Once the admittance matrix of the two-port network is obtained, it is transformed into an equivalent π-section, as depicted in Fig. 5. Finally, the vector fitting algorithm in MATLAB is utilized to derive the s-domain transfer functions for the elements of the admittance matrices, $\mathbf{Y}_{\mathrm{T1}}$, $\mathbf{Y}_{\mathrm{T2}}$, and $\mathbf{Y}_{\mathrm{T3}}$.

E. Admittance Model of the WPP and its Verification

Once the admittance/impedance models of all the components of the WPP are obtained, the equivalent admittance of the WPP at the terminal T1 can be obtained from the series/parallel relations of the components as

$$\begin{aligned}\mathbf{Y}_{\mathrm{WPP}} = &[[[\mathbf{Y}_{\mathrm{WT}}^{-1} + \mathbf{Z}_{\mathrm{tr2}}]^{-1} + \mathbf{Y}_{\mathrm{T3}}]^{-1} + \mathbf{Y}_{\mathrm{T2}}^{-1}]^{-1} + \mathbf{Y}_{\mathrm{T1}} \\ &+ [\mathbf{Y}_{\mathrm{GFM/GFL}}^{-1} + \mathbf{Z}_{\mathrm{tr1}}]^{-1} + [\mathbf{Z}_{\mathrm{R1}}]^{-1}.\end{aligned} \tag{30}$$

To verify the analytically derived $\mathbf{Y}_{\mathrm{WPP}}$, a detailed time-domain simulation of the WPP network shown in Fig. 2, including all control loops (implemented in discrete time) is used and a stiff-grid connection (i.e., $L_{\mathrm{g}} = R_{\mathrm{g}} = 0$) is assumed. A similar methodology as described earlier is used to obtain $\mathbf{Y}_{\mathrm{WPP}}$ from the simulation model.

The system and control parameters used for the WT and ES-STATCOM are listed in Table I and II, respectively. The simulation tests are performed with the following conditions; the WPP is operated at half of its nominal value, the reactive power set-point of the WTs and active power set-point of the ES-STATCOM is zero, and the voltage at the connection point of the ES-STATCOM is regulated at its rated value. As an example, Fig. 6 shows the frequency response of the real and imaginary parts of the first row elements of $\mathbf{Y}_{\mathrm{WPP}}$ obtained analytically (solid-blue curves) and from the detailed simulation model (dotted-red curves) for the two cases (ES-STATCOM in GFM/GFL mode). The results show a very good match between the simulation and the analytical frequency characteristics, thereby verifying the validity of the obtained analytical model.

TABLE I
MAIN SYSTEM AND CONTROL PARAMETERS FOR THE WT

System parameters		Control parameters	
S_{N}	480 MVA (1.0 pu)	α_{cc}	$2\pi500$ rad/s
E_{N}	0.69 kV (1.0 pu)	α_{ff}	$2\pi500$ rad/s
ω_{N}	314.16 rad/s	α_{dc}	$2\pi5$ rad/s
R_{f}	0.012 pu	α_{qc}	$2\pi5$ rad/s
L_{f}	0.12 pu	α_{PLL}	$2\pi5$ rad/s

TABLE II
MAIN SYSTEM AND CONTROL PARAMETERS FOR THE ES-STATCOM

System parameters		Control parameters	
S_{N}	112 MVA (1.0 pu)	α_{pc}	$2\pi5$ rad/s
E_{N}	33.0 kV (1.0 pu)	α_{vc}	$2\pi1$ rad/s
ω_{N}	314.16 rad/s	α_{hpf}	$2\pi5$ rad/s
R_{f}	0.005 pu	α_{fmv}	$2\pi100$ rad/s
L_{f}	0.05 pu	R'_{a}	0.1 pu

IV. COMPARATIVE ANALYSIS OF THE SMALL-SIGNAL STABILITY OF THE GRID-CONNECTED WPP

Using the equivalent circuit shown in Fig. 7, the line-current dynamics can be expressed in scalar form as

$$\begin{bmatrix} i^s_{\mathrm{g,d}} \\ i^s_{\mathrm{g,q}} \end{bmatrix} = [I + \mathbf{Y}_{\mathrm{WPP}}\mathbf{Z}_{\mathrm{g}}]^{-1} \left(\begin{bmatrix} i^s_{\mathrm{Neq,d}} \\ i^s_{\mathrm{Neq,q}} \end{bmatrix} - \mathbf{Y}_{\mathrm{WPP}} \begin{bmatrix} e^s_{\mathrm{s,d}} \\ e^s_{\mathrm{s,q}} \end{bmatrix} \right), \tag{31}$$

where $\mathbf{Z}_{\mathrm{g}}$ denotes the impedance matrix of the grid. For the investigated system, the current and voltage inputs as well as the individual subsystems are stable and therefore the stability of the interconnected system in (31) can be studied using the total open-loop gain, $\mathbf{G}_{\mathrm{OL}} = \mathbf{Y}_{\mathrm{WPP}}\mathbf{Z}_{\mathrm{g}}$ through frequency-domain analysis.

For a generic multiple-input-multiple-output (MIMO) system as the one in (31), the generalized Nyquist criterion for the open-loop transfer matrix can be used to study its closed-loop

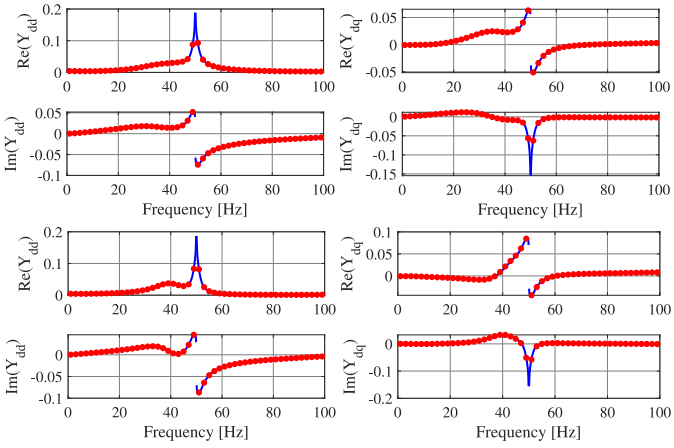

Fig. 6. First row elements of the input-admittance matrix, $\mathbf{Y}_{\mathrm{WPP}}$, obtained analytically (solid-blue curves) and from simulation model (dotted-red curves) for the case with ES-STATCOM in GFM mode (top) and GFL mode (bottom).

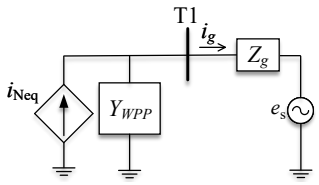

Fig. 7. Equivalent circuit representation of an aggregated model of a grid-connected WPP.

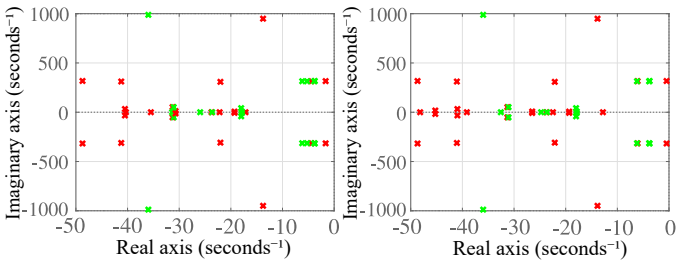

Fig. 8. Dominant poles of $\mathbf{Y}_{\mathrm{WPP}}$ with ES-STATCOM in GFM mode (green markers) and GFL mode (red markers) for different values of the voltage controller bandwidth. Left: α_{vc} =2π1 rad/s; right; α_{vc} =2π10 rad/s.

stability. The Nyquist curve is obtained by plotting together the frequency response of the eigenvalues of $\mathbf{G}_{\mathrm{OL}}$. In this criterion, given the stability of the two subsystems—namely, the WPP and the onshore grid—represented by their transfer matrices $\mathbf{Y}_{\mathrm{WPP}}$ and $\mathbf{Z}_{\mathrm{g}}$ respectively, the closed-loop (interconnected) system described in (31) is stable if the Nyquist curve does not encircle the point (-1, 0). In general, the onshore AC transmission grid, represented by its Thévenin equivalent, does not have any right-half plane poles, and hence, it is stable. Furthermore, by analyzing the dominant poles of $\mathbf{Y}_{\mathrm{WPP}}$ shown in Fig. 8, it can be understood that for the case studies considered in this section, the two subsystems are stable.

Figure 9 shows the generalized Nyquist plot of $\mathbf{G}_{\mathrm{OL}}$ when ES-STATCOM is in GFM mode (green curves) and GFL mode (red curves) for two different values of the voltage controller bandwidth. The grid impedance corresponding to SCR of 1.5 at the onshore terminal T1 is selected for the case

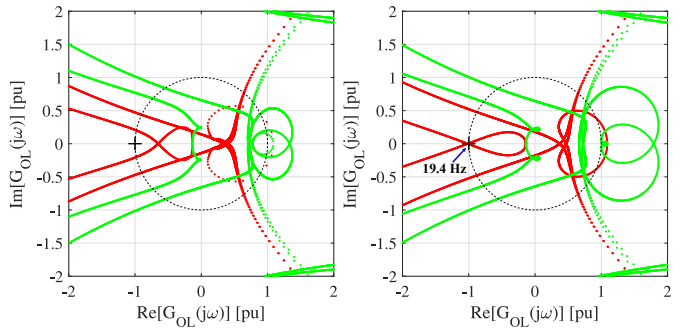

Fig. 9. Generalized Nyquist plot of $\mathbf{G}_{\mathrm{OL}} = \mathbf{Y}_{\mathrm{WPP}}\mathbf{Z}_{\mathrm{g}}$ with ES-STATCOM in GFM mode (green curves) and GFL mode (red curves) for different values of the voltage controller bandwidth. Left: $\alpha_{\mathrm{vc}} = 0.02$ pu; right: $\alpha_{\mathrm{vc}} = 0.2$ pu.

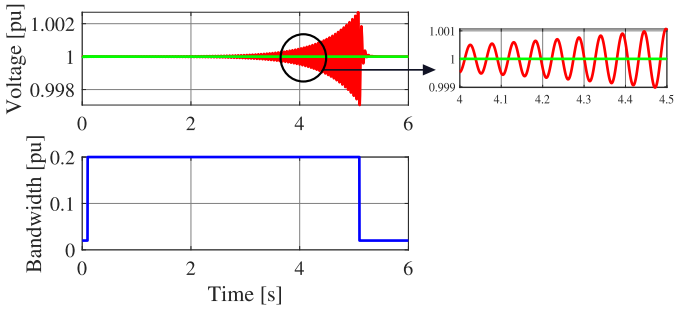

Fig. 10. Impact of the voltage controller bandwidth. Top: voltage magnitude at terminal T1 of the WPP with ES-STATCOM in GFM mode (green curve) and GFL mode (red curve); bottom: bandwidth of the voltage controller.

study here. It can be observed from the left side generalized Nyquist plot that with $\alpha_{\mathrm{vc}} = 0.02$ pu and the ES-STATCOM operated in GFL mode, both the gain and phase margins of the interconnected system are reduced compared to when the ES-STATCOM is operated in GFM mode. Furthermore, increasing the bandwidth of the voltage controller to $\alpha_{\mathrm{vc}} = 0.2$ pu renders the interconnected system unstable when the ES-STATCOM is operated in GFL mode as can be observed from the right side generalized Nyquist plot.

To verify the theoretical findings presented above, detailed time-domain simulations are performed in PSCAD. An offshore wind farm configuration comprising three radials is considered due to aforementioned limitation in the number of electrical nodes in the simulation software. System and control parameters listed in Table I and II are used for the WT and ES-STATCOM, respectively. Figure 10 depicts the impact of varying the loop bandwidth of the voltage controller on the system stability for the two cases. From the theoretical analysis conducted above, instability is expected for the case with the ES-STATCOM in GFL mode when $\alpha_{\mathrm{vc}} = 0.2$ pu. It can be observed from the plot of the voltage magnitude at terminal T1 of the WPP, shown in Figure 10, that with the ES-STATCOM operated in GFL mode (red curve), oscillations commence when $\alpha_{\mathrm{vc}} = 0.2$ pu, while the system stabilizes when the loop bandwidth is reduced back to $\alpha_{\mathrm{vc}} = 0.02$ pu. The frequency of the oscillations matches with the one obtained from the generalized Nyquist plot in Fig. 9 for the unstable case. Furthermore, it can be observed from Fig. 10 that increasing the bandwidth of the voltage controller while operating the ES-STATCOM in GFM mode (green curve) does not destabilize the system, which aligns with the analysis from the generalized Nyquist plot in Fig. 9. The results obtained from electromagnetic transient (EMT) simulations thus validate the correctness and acceptable accuracy of the small-signal models.

V. Analysis of Grid-Forming Capabilities of the WPP

The emergence of grid-forming capability requirements is a recent development in grid codes [13]. Currently, there is no universally accepted method for demonstrating the provision of these capabilities. In [15], various approaches

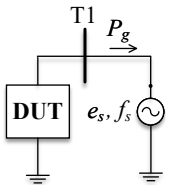

Fig. 11. Test network for generating NFP plot using time-domain simulation.

such as small-signal and impedance-based analyses, root mean square (RMS), electromagnetic transient (EMT) time-domain simulations, and real-time simulations are discussed as means to assess compliance with grid-forming requirements and to verify the absence of adverse control interactions. Guidelines accompanying the German HVDC standard VDE-AR-N 4131 contain a set of scenarios for time-domain simulations with predefined performance envelopes for acceptable behavior [27]. In contrast, [28] takes a different approach, showcasing the magnitude and phase of active-power response to a disturbance in grid voltage frequency and comparing it to a synchronous machine's (SM) response in a network frequency perturbation (NFP) plot. This method has received further discussion in [29] and has been acknowledged by National Grid ESO as a means to demonstrate grid-forming performance and the absence of adverse control interactions [30]. Consequently, in this study, the NFP plot is employed to determine whether the WPP offers grid-forming capabilities at the point of grid-connection (POC).

A. Methodology to Generate and Interprete NFP Plots

NFP plots in this work are generated by performing time-domain simulations with a subsequent Fourier analysis of the results [2]. In order to obtain the NFP plot from time-domain simulation, a device under test (DUT) is placed in a test environment as illustrated in Fig. 11, and its active-power response when subjected to frequency perturbation is recorded. The frequency perturbation is generated by varying the frequency of the source voltage, f_s in sinusoidal fashion according to

$$f_\mathrm{s}(t) = f_\mathrm{N} + \Delta f_\mathrm{s} \cos(2\pi f_\mathrm{NFP} t + \phi_\mathrm{NFP,f}), \tag{32}$$

where f_N is the nominal frequency, and the perturbation is characterized by its amplitude Δf_s, modulation frequency f_NFP and phase $\phi_\mathrm{NFP,f}$. The modulation frequency is swept across the range of interest, typically between 0.01 and 30 Hz. To prevent saturation in the control loops of the DUT, Δf_s should be kept small. The DUT responds to the frequency variations with a modulated active-power response, which is characterized by

$$P_\mathrm{g}(t) = P_\mathrm{set} + \Delta P_\mathrm{g} \cos(2\pi f_\mathrm{NFP} t + \phi_\mathrm{NFP,P}), \tag{33}$$

[2] As mentioned in [22], it is also possible to conduct an analysis of the linearized system's closed-loop transfer function from the grid-voltage frequency to the tested unit's active-power variation.

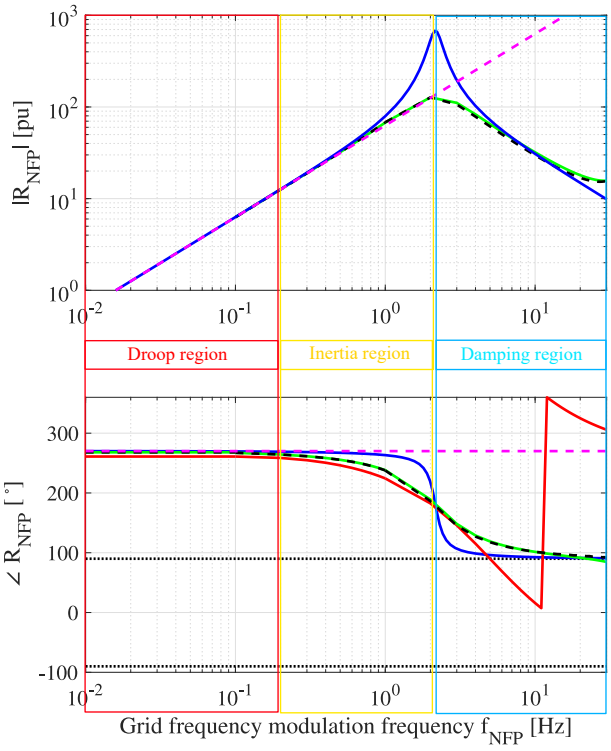

Fig. 12. The NFP plot of an ideal SC (blue curves), a GFM converter (green curves), GFL converter (red curve) and the WPP with a GFM ES-STATCOM (dashed-black curves). The amplitude response of the GFL converter is below the y-axis' lower limit and therefore is omitted from the figure.

where per-unit quantities are used for the power. This allows to calculate the NFP response as

$$\underline{R}_\mathrm{NFP} = \frac{\Delta P_\mathrm{g} \angle \phi_\mathrm{NFP,P}}{\frac{\Delta f_\mathrm{s}}{f_\mathrm{N}} \angle \phi_\mathrm{NFP,f}}, \tag{34}$$

employing a Fourier analysis of the measured or simulated active power P_g to calculate the amplitude ΔP_g and phase $\phi_\mathrm{NFP,P}$ of the active-power variation. This response can then be plotted similar to a Bode diagram with separate plots for magnitude and phase, usually on logarithmic axes.

Figure 12 shows the NFP plots for an ideal synchronous condenser (SC), a GFM converter, and a GFL converter, all of similar ratings (as that of the ES-STATCOM in the considered WPP) for a fair comparison. In the plot, the SC's response is represented in blue, the GFM converter in green, and the GFL converter in red. The SC's response exhibits four distinctive features. Firstly, when the machine provides any frequency droop, the response's magnitude should approach the droop constant, and the phase should approach a value of 180° for $f_\mathrm{NFP} \to 0$. In cases where, like this SC, no droop is provided, the magnitude should tend towards 0 instead. The frequency range where droop behavior dominates is typically defined as 0 to 0.2 Hz. The second key feature relates to the provision of inertia. The response of a pure inertial response, without droop, rotor resonance, or damping, is referred to as the inertia asymptote and is represented by the dashed magenta curve. Approaching the inertia asymptote in both

magnitude and phase within the inertia region (typically 0.2 to 2 Hz) signifies the provision of an inertial response. As seen in the figure, the SC approaches the inertia asymptote due to its mechanical inertia. The third key feature is a resonance that occurs at the characteristic frequency of the second-order transfer function describing the system behavior. Typically, this resonance falls within a frequency range of 1 and 3 Hz, depending on factors such as the device's inertia constant, damping coefficient, and the total reactance between the device and the grid's Thévenin voltage. The low damping coefficient characteristic of synchronous machines results in a pronounced resonance peak and a steep phase transition in the SC's response. The fourth key feature is the response to rapid changes or oscillations in grid frequency or voltage phase angle, characterized by the response in the damping region (above 2.0 Hz). For a SM, this response is characterized by a continuous decrease in magnitude, coupled with the phase approaching $90°$, indicating the provision of synchronizing torque.

By examining the adherence of an investigated device to these features that characterize the NFP plots of SM, it is possible to assess whether and to what extent grid-forming capabilities are provided. As can be observed from the red curve in Fig. 12, the GFL converter does not exhibit droop or inertial response, as the magnitude of the response is too low. Concerning the damping region, it should be noted that the phase angle of the response drops below $90°$ and becomes negative for frequencies above 10 Hz, indicating negative damping and synchronizing power components. In contrast, the GFM converter, designed without a droop response, closely resembles the SC's response in all four key features. The main distinctions are a less pronounced resonance peak and a smoother phase transition, attributed to the higher damping coefficient in the converter.

B. NFP Plots of the WPP

The behaviour of the WPP with a GFM ES-STATCOM is assessed through its NFP plot. This plot is generated by introducing a frequency perturbation in the voltage at POC denoted as T1 in Fig. 2. To facilitate comparison with previous example cases, the measured active power is normalized with respect to the ES-STATCOM's rating of 112 MVA. The resulting response is represented by the dashed black curves in Fig. 12. It can be observed that the WPP's response closely aligns with the behavior of a pure GFM converter, depicted by the green curves, and exhibits a similar adherence to the four key characteristics observed in the SC's response. A comprehensive study, involving various WT operating points and different ES-STATCOM sizes employing DCCV type of GFM control, revealed only minimal impact on the WPP's NFP response. In summary, the NFP plot confirms that the presence of a GFM ES-STATCOM at the WPP's grid connection point can impart grid-forming behavior to the WPP at that specific location.

VI. Conclusions

This paper has investigated the influence of converter control methods in an ES-STATCOM responsible for voltage control and stability enhancement within an offshore WPP connected to the grid via HVAC transmission network. Through the application of the generalized Nyquist criterion to a linearized system model, the study has shown that employing GFM control in the ES-STATCOM yields an enhanced stability margin compared to GFL control. Subsequently, the study has utilized NFP plot to assess whether the WPP exhibits GFM characteristics at the POC when the ES-STATCOM operates in GFM and the WTs use GFL control mode. A comparison with the NFP responses of a SC and a pure GFM converter illustrates that the WPP is indeed capable of manifesting GFM behavior, given the selected relative size of the GFM ES-STATCOM. Further investigations have affirmed that this conclusion holds regardless of the operating point of the WTs.

VII. Appendix

$$
\begin{aligned}
A_{\mathrm{e}} &= \sin^2\theta_{\mathrm{L0}} e^s_{\mathrm{g,d0}} - \sin\theta_{\mathrm{L0}}\cos\theta_{\mathrm{L0}} e^s_{\mathrm{g,q0}},\\
B_{\mathrm{e}} &= \cos^2\theta_{\mathrm{L0}} e^s_{\mathrm{g,q0}} - \sin\theta_{\mathrm{L0}}\cos\theta_{\mathrm{L0}} e^s_{\mathrm{g,d0}},\\
E_{\mathrm{g0}} &= \cos\theta_{\mathrm{L0}} e^s_{\mathrm{g,d0}} + \sin\theta_{\mathrm{L0}} e^s_{\mathrm{g,q0}};\\
A_{\mathrm{i}} &= \sin^2\theta_{\mathrm{L0}} i^s_{\mathrm{f,d0}} - \sin\theta_{\mathrm{L0}}\cos\theta_{\mathrm{L0}} i^s_{\mathrm{f,q0}},\\
B_{\mathrm{i}} &= \cos^2\theta_{\mathrm{L0}} i^s_{\mathrm{f,q0}} - \sin\theta_{\mathrm{L0}}\cos\theta_{\mathrm{L0}} i^s_{\mathrm{f,d0}},\\
I_{\mathrm{f0}} &= \cos\theta_{\mathrm{L0}} i^s_{\mathrm{f,d0}} + \sin\theta_{\mathrm{L0}} i^s_{\mathrm{f,q0}};\\
A_{\mathrm{d}} &= \sin^2\theta_{\mathrm{L0}} e^s_{\mathrm{c,d0}} - \sin\theta_{\mathrm{L0}}\cos\theta_{\mathrm{L0}} e^s_{\mathrm{c,q0}},\\
B_{\mathrm{d}} &= \cos^2\theta_{\mathrm{L0}} e^s_{\mathrm{c,q0}} - \sin\theta_{\mathrm{L0}}\cos\theta_{\mathrm{L0}} e^s_{\mathrm{c,d0}},\\
E_{\mathrm{c0}} &= \cos\theta_{\mathrm{L0}} e^s_{\mathrm{c,d0}} + \sin\theta_{\mathrm{L0}} e^s_{\mathrm{c,q0}};\\
G_{\mathrm{PLL}} &= \frac{F_{\mathrm{PLL}}}{(1+F_{\mathrm{PLL}})E_{\mathrm{g0}}}
\end{aligned}
$$

$$
\mathbf{G}_{\mathrm{Qdc}} = \begin{bmatrix} \frac{K_{\mathrm{p,dc}}\mathbf{G}_{\mathrm{f}}}{E_{\mathrm{g0}}C_{\mathrm{dc}}s} \\ \frac{-G_{\mathrm{qc}}e^s_{\mathrm{g,q0}}}{E_{\mathrm{N}}} \quad \frac{G_{\mathrm{qc}}e^s_{\mathrm{g,d0}}}{E_{\mathrm{N}}} \end{bmatrix}
$$

$$
\mathbf{G}_{\mathrm{f}} = \begin{bmatrix} e^s_{\mathrm{c,d0}} & e^s_{\mathrm{c,q0}} \end{bmatrix} + \begin{bmatrix} i^s_{\mathrm{f,d0}} & i^s_{\mathrm{f,q0}} \end{bmatrix} \overbrace{\begin{bmatrix} R_{\mathrm{f}}+sL_{\mathrm{f}} & -\omega_{\mathrm{N}}L_{\mathrm{f}} \\ \omega_{\mathrm{N}}L_{\mathrm{f}} & R_{\mathrm{f}}+sL_{\mathrm{f}} \end{bmatrix}}^{\mathbf{Z}_{\mathrm{f}}}
$$

$$
\mathbf{Y}_{\mathrm{Qdc}} = \begin{bmatrix} \frac{K_{\mathrm{p,dc}}i^s_{\mathrm{f,d0}}}{E_{\mathrm{g0}}C_{\mathrm{dc}}s} - \frac{P_{\mathrm{w0}}H_{\mathrm{dc}}e^s_{\mathrm{g,d0}}}{E^3_{\mathrm{g0}}} & \frac{K_{\mathrm{p,dc}}i^s_{\mathrm{f,q0}}}{E_{\mathrm{g0}}C_{\mathrm{dc}}s} - \frac{P_{\mathrm{w0}}H_{\mathrm{dc}}e^s_{\mathrm{g,q0}}}{E^3_{\mathrm{g0}}} \\ \frac{G_{\mathrm{qc}}i^s_{\mathrm{f,q0}}}{E_{\mathrm{N}}} & \frac{-G_{\mathrm{qc}}i^s_{\mathrm{f,d0}}}{E_{\mathrm{N}}} \end{bmatrix}
$$

$$
\mathbf{G}_{\mathrm{PV}} = \begin{bmatrix} \frac{-G_{\mathrm{pc}}e^s_{\mathrm{g,d0}}}{E_{\mathrm{N}}} & \frac{-G_{\mathrm{pc}}e^s_{\mathrm{g,q0}}}{E_{\mathrm{N}}} \\ 0 & 0 \end{bmatrix},
$$

$$
\mathbf{Y}_{\mathrm{PV}} = \begin{bmatrix} \frac{-G_{\mathrm{pc}}i^s_{\mathrm{f,d0}}}{E_{\mathrm{N}}} & \frac{-G_{\mathrm{pc}}i^s_{\mathrm{f,q0}}}{E_{\mathrm{N}}} \\ \frac{-G_{\mathrm{vc}}e^s_{\mathrm{g,d0}}}{E_{\mathrm{g0}}} & \frac{-G_{\mathrm{vc}}e^s_{\mathrm{g,q0}}}{E_{\mathrm{g0}}} \end{bmatrix}.
$$

References

[1] International Energy Agency, "Renewable Energy Market Update - June 2023," 2023.

[2] Global Wind Energy Council, "Global Wind Report 2023," Mar. 27, 2023.

[3] R. Perveen, N. Kishor, and S. R. Mohanty, "Off-shore wind farm development: Present status and challenges," *Renewable and Sustainable Energy Reviews*, vol. 29, Jan. 2014.

[4] S. Hardy, K. Van Brusselen, S. Hendrix, D. Van Hertem, and H. Ergun, "Techno-economic analysis of HVAC, HVDC and OFAC offshore wind power connections," in *2019 IEEE Milan PowerTech*, 2019.

[5] M. Beza and M. Bongiorno, "Identification of resonance interactions in offshore-wind farms connected to the main grid by MMC-based HVDC system," *International Journal of Electrical Power & Energy Systems*, vol. 111, Oct. 2019.

[6] E. Ebrahimzadeh, F. Blaabjerg, X. Wang, and C. L. Bak, "Harmonic Stability and Resonance Analysis in Large PMSG-Based Wind Power Plants," *IEEE Transactions on Sustainable Energy*, vol. 9, no. 1, Jan. 2018.

[7] Ł. H. Kocewiak, I. A. Aristi, B. Gustavsen, and A. Hołdyk, "Modelling of wind power plant transmission system for harmonic propagation and small-signal stability studies," *IET Renewable Power Generation*, vol. 13, no. 5, 2019.

[8] J. Castaneda, J. Enslin, D. Elizondo, N. Abed, and S. Teleke, "Application of STATCOM with energy storage for wind farm integration," in *IEEE PES T&D 2010*, Apr. 2010.

[9] M. Marques, R. Castro, and M. Almeida, "Connection of offshore wind parks: HVAC and HVDC-LCC links with STATCOM," in *11th International Conference on Electrical Power Quality and Utilisation*, Oct. 2011.

[10] S. W. Ali *et al.*, "Offshore Wind Farm-Grid Integration: A Review on Infrastructure, Challenges, and Grid Solutions," *IEEE Access*, vol. 9, 2021.

[11] Hitachi Energy, "Hitachi Energy wins order to connect one of the world's largest offshore wind farms to the UK power grid," Jul. 14, 2022.

[12] 50Hertz Transmission. "Kriegers Flak – Combined Grid Solution." (), [Online]. Available: https : / / www . 50hertz . com / en / Grid / Griddevelopement / Concludedprojects / CombinedGridSolution (visited on 09/08/2023).

[13] P. Imgart, M. Beza, M. Bongiorno, and J. R. Svensson, "An Overview of Grid-Connection Requirements for Converters and Their Impact on Grid-Forming Control," in *2022 24th European Conference on Power Electronics and Applications (EPE'22 ECCE Europe)*, Sep. 2022.

[14] J. Matevosyan *et al.*, "Grid-Forming Inverters: Are They the Key for High Renewable Penetration?" *IEEE Power and Energy Magazine*, vol. 17, no. 6, Nov. 2019.

[15] ENTSO-E, "High Penetration of Power Electronic Interfaced Power Sources and the Potential Contribution of Grid Forming Converters," 2020.

[16] Z. Yang, C. Shen, L. Zhang, M. Crow, and S. Atcitty, "Integration of a StatCom and battery energy storage," in *2001 Power Engineering Society Summer Meeting. Conference Proceedings (Cat. No.01CH37262)*, vol. 3, Jul. 2001.

[17] L. Huang, C. Wu, D. Zhou, and F. Blaabjerg, "Mixed Grid-Forming and Grid-Following Inverters with Secondary Control Providing Fast Voltage and Frequency Support," 2023.

[18] J. Hjerrild *et al.*, "Hornsea projects one and Two–Design and execution of the grid connection for the world's largest offshore wind farms," in *Cigre Symposium Aalborg*, 2019.

[19] S. K. Chaudhary *et al.*, "Black Start Service from Offshore Wind Power Plant using IBESS," in *2021 IEEE Madrid PowerTech*, Jun. 2021.

[20] S. K. Chaudhary *et al.*, "Islanded Operation of Offshore Wind Power Plant using IBESS," in *2021 IEEE Power & Energy Society General Meeting (PESGM)*, Jul. 2021.

[21] J. Dakic, M. Cheah-Mane, O. Gomis-Bellmunt, and E. Prieto-Araujo, "Hvac transmission system for offshore wind power plants including mid-cable reactive power compensation: Optimal design and comparison to vsc-hvdc transmission," *IEEE Transactions on Power Delivery*, vol. 36, no. 5, 2021.

[22] A. Narula, "Grid-forming wind power plants," Chalmers University of Technology, 2023.

[23] M. Beza and M. Bongiorno, "On the Risk for Subsynchronous Control Interaction in Type 4 Based Wind Farms," *IEEE Transactions on Sustainable Energy*, vol. 10, no. 3, 2019.

[24] E. Behrouzian, M. Bongiorno, J. R. Svensson, and A. Mohanaveeramani, "A novel capacitor-voltage balancing strategy for double-y statcom under unbalanced operations," *IEEE Transactions on Industry Applications*, vol. 57, no. 3, 2021.

[25] L. Harnefors, M. Hinkkanen, U. Riaz, F. M. M. Rahman, and L. Zhang, "Robust analytic design of power-synchronization control," *IEEE Transactions on Industrial Electronics*, vol. 66, no. 8, 2019.

[26] G. Francis, R. Burgos, D. Boroyevich, F. Wang, and K. Karimi, "An algorithm and implementation system for measuring impedance in the d-q domain," in *2011 IEEE Energy Conversion Congress and Exposition*, 2011.

[27] Verband der Elektrotechnik Elektronik Informationstechnik e. V., *VDE FNN Guideline FNN Guideline: Grid forming behaviour of HVDC systems and DC-connected PPMs*, 2020.

[28] M. Yu *et al.*, "Instantaneous penetration level limits of non-synchronous devices in the British power system," *IET Renewable Power Generation*, vol. 11, no. 8, 2017.

[29] ENTSO-E, "High Penetration of Power Electronic Interfaced Power Sources (HPoPEIPS)," 2017.

[30] National Grid ESO, *Final Modification Report GC0137: Minimum Specification Required for Provision of GB Grid Forming (GBGF) Capability*, Nov. 11, 2021.